# Evaluating the oxidation kinetic parameters of gasoline direct injection soot from thermogravimetric analysis experiments

P. Piqueras*[a], E. J. Sanchis[a], J. M. Herreros[b], A. Tsolakis[b]

[a]*CMT-Motores Térmicos, Universitat Politècnica de València, Camino de Vera s/n, 46022 Valencia, Spain.*
[b]*Deparment of Mechanical Engineering, University of Birmingham, Edgbaston B15 2TT, UK.*

**Abstract**

The abatement of particulate matter in gasoline direct injection (GDI) engines requires the use of particulate filters. In turn, the optimisation of their regeneration is based on a deep knowledge of the soot oxidation behaviour. The determination of the intrinsic kinetic parameters of GDI soot is explored based on thermogravimetric analysis (TGA) and reaction rate modelling. New understanding on the oxidation of GDI soot is provided enabling an accurate prediction in a wide range of temperature and $O_2$ concentration. Firstly, the dependence of the soot reaction order on the boundary conditions is discussed. The analysis of the Arrhenius equation parameters reveals variable $O_2$ reaction order. It leads to consider the effect of mass transfer and adsorption (Langmuir and Dubinin-Radushkevich isotherms) as reaction rate limiters. Combined with the soot reaction order approach, the prediction ability of the proposed model is assessed in an extended range of isothermal and non-isothermal TGA experiments.

*Keywords:* Gasoline direct injection, soot, TGA, oxidation, adsorption

## 1. Introduction

Anthropogenic particulate matter (PM) is one of the most harmful emissions for the environment and human health (Manousakas et al., 2019). Fine particulate matter, usually ranged as particles with sizes smaller than 2.5 $\mu m$, are more prone to cause respiratory diseases (Feng et al., 2019).

*Corresponding author. Tel.: +34 96 3877650.
*Email address:* pedpicab@mot.upv.es (P. Piqueras*)

*March 2, 2021*

On this concern, road transport arises as one of the main contributors of PM emissions (Charron et al., 2007) from both non-exhaust (tyre, brake, road surface) and exhaust sources (Singh et al., 2020). Although this pollutant emission has traditionally been related to compression ignition engines, it is becoming more important in modern gasoline direct injection (GDI) engines (Pfau et al., 2018).

GDI engines provide accurate control on the combustion process (Alkidas, 2007), what leads to the combustion efficiency increase (Zhang et al., 2018). However, this combustion strategy causes an increase of the raw particulate matter emission in comparison to indirect injection (Bahreini et al., 2015). Taking into account the current emission limits for the number of emitted particles in gasoline engines (715/2007bis, 2007), manufacturers and researchers are driving relevant efforts to the understanding of the formation, inhibition and abatement of particulate matter in GDI engines (Zimmerman et al., 2016). Concerning control techniques, besides combustion related aspects, such as the fuel (Soriano et al., 2017), the lubricant composition (Maricq et al., 2012) or the injection pattern (Jiaqiang et al., 2018), the use of wall-flow particulate filters (PFs) is the most promising solution to reduce the particulate matter emission from GDI engines (Joshi, 2019).

PFs have been widely studied for Diesel applications covering the fundamentals of their operation. Pressure drop (Payri et al., 2011), soot and ash loading impact (Zhang et al., 2017), filtration efficiency (Serrano et al., 2016) and regeneration (Macián et al., 2019) have been studied combining experimental and modelling tools. From this basis, the study of gasoline particulate filters (GPFs) is focused on the requirements of the substrate in comparison with the diesel case (Belot et al., 2020). This is largely conditioned by the characteristics of the emitted particulate matter regarding ash content (Rubino et al., 2017), particle size distribution (Fan et al., 2019) or reactivity, as well as exhaust flow properties (mass flow rate, temperature and composition) (Kong et al., 2019).

The soot reactivity, which presents dependence on the soot origin as regards fuel, combustion process, and the specific operating conditions (Ess et al., 2016), is a primary property that affects the dynamics of the PF regeneration (Macián et al., 2019). Several experimental techniques (Lapuerta et al., 2020), such as X-ray diffraction (Jian et al., 2020) or thermogravimetric analysis (TGA) (Rodríguez-Fernández et al., 2011), can be used for its determination. TGA is based on the variation of the sampled mass in an environment with controlled temperature and gas composition during the reaction (Wang et al., 2017). It guides a comprehensive understanding of the processes governing the oxidation and, hence, the definition of the soot kinetic parameters (Lee et al., 2013). The most common approach to analyse TGA results consists of the application of kinetic models for solid-state reactions. These models describe the reaction rate apparently separating the contributions from particle and gas (Lapuerta et al., 2020).

The influence of soot on the reaction rate is analysed by means of solid-state reaction models (Sánchez-Jiménez et al., 2008). In most cases, the dependence on the soot mass is expressed as a function of a reaction order or a model describing the particle contraction or the diffusion limitations (Khawam and Flanagan, 2006). Although the oxidation kinetics of the GDI soot has been analysed in the literature (Gaddam and Vander Wal, 2013), the GDI soot first-order kinetics is usually assumed to compare with soot generated by other sources: Luo et al. (2015) analysed soot from gasoline and fuel blends E10 and E20; Wang et al. (2014) studied the properties of soot generated by the combustion of gasoline, ethanol and 2.5-dimethylfuran; Wang-Hansen et al. (2013) evaluated the reactivity of soot from different sources including diesel, Printex U and gasoline applying Port Fuel Injection (PFI) and GDI combustion; Choi et al. (2015) assumed zero-order kinetics with respect to $O_2$ obtaining a soot reaction order ranging between 0.5 and 1. According to their results, the oxidation kinetics of GDI soot cannot be modelled with typical kinetic expressions for carbonaceous soot.

In particular, Bogarra et al. (2018), who presented the GDI soot experimental results used in this study, proposed a procedure to determine the kinetic parameters using TGA isothermal exper-

iments and the Arrhenius equation. The best fitting was obtained for a soot reaction order equal to 0.81 assuming $O_2$ first-order kinetics, which was imposed to describe the dependence of the soot oxidation rate on the gaseous reactant. This is the most widespread assumption for diesel (Deng et al., 2017), GDI soot (Luo et al., 2015) and carbon black (Jaramillo et al., 2015). However, Hurt et al. (2005) revealed the prevalence of $O_2$ first-order kinetics but also evidenced fractional orders. In this regard, Bogarra et al. (2018) also showed that the decrease of the $O_2$ reaction order till 0.6 did not affected the ability to meet a good fitting but impacted on the determination of the soot reaction order and pre-exponential factor.

In this work, the determination of the kinetic parameters that describe the dynamics of the GDI soot oxidation is discussed by means of a step-by-step procedure applied to TGA tests. The proposed reaction rate expression and the influence of the involved parameters are analysed taking as a reference isothermal TGA tests that comprise a wide range in temperature and $O_2$ concentration. Firstly, the problem is divided into the classical dependence on the solid-state (soot) reaction model and a kinetic term determined by the gaseous reactant concentration ($O_2$) and the temperature. The purpose is to perform an independent analysis of these contributions to the soot oxidation. An initial breakdown of the experimental data shows that the cylinder contracting area reaction model might be assumed as an accurate theoretical representation of the oxidation behaviour for lean combustion conditions. However, the soot reaction order decreases for very low $O_2$ concentration, representative of engine stoichiometric combustion. As regards the influence of the gaseous reactant, the classical assumption of first-order kinetics is found to vary the activation energy and pre-exponential factor as a function of the $O_2$ concentration. Therefore, a reaction rate expression is proposed to distinguish the intrinsic reactivity, the influence of the mass transfer and the oxygen adsorption, which is evaluated applying the Langmuir and Dubinin-Radushkevich isotherms. As a final step, the proposed reaction rate expression is validated against additional low temperature isothermal TGA tests and in non-isothermal experiments defined by different heating rates. For first time, this work proposes a soot oxidation model combining oxygen adsorption and oxidation

being validated for a wide range of operating conditions representative from regular regeneration of GPFs under real driving operation.

## 2. Materials and methods

The soot samples used in this work were obtained by Bogarra et al. (2018) in a GDI engine whose characteristics are detailed in Table 1. The engine was tested with standard EN228 gasoline, whose properties are summarized in Table 2, at 2100 rpm and 4.7 bar IMEP (Bogarra et al., 2016) without exhaust gas recirculation (EGR).

Table 1: Main engine characteristics.

| | |
|---|---|
| Compression ratio | 10:1 |
| Number of cylinders | 4 in line |
| Number of valves | 4 per cylinder |
| Displaced volume | 1998 $cm^3$ |
| Bore | 87.5 mm |
| Stroke | 83.1 mm |
| Turbocharger | Waste-gaste turbine |
| Rated power @ speed | 149 kW @6000 rpm |
| Rated torque @ speed | 300 Nm @ 1750 – 4500 rpm |

Bogarra et al. analysed the soot nanostructure (Bogarra et al., 2017a) and fractal dimension (Bogarra et al., 2017b). The structure of the primary particles was similar to that of diesel soot. However, opposite to diesel case, the use of EGR did not affect the soot nanostructure. The three-way catalyst did not cause any change in the soot nanostructural characteristics either. With respect to TGA tests, Bogarra et al. (2018) explored several methods for soot collection in GDI engines. In the case of the soot samples analysed in this work, raw exhaust gas was by-passed and driven to a wall-flow particulate mini-filter. The monolithic structure was placed into a reactor thermally stabilised at 450°C. After the test, the soot was recovered by blowing purified air from the outlet channels into a container.

Once the soot mass samples were obtained, the TGA tests were carried out in a TG analyser model Pyris from Perkin Elmer, whose precision is ±5°C for temperature control and 0.001% for

Table 2: EN228 gasoline properties.

| | | |
|---|---|---|
| Density at 15°C | [kg/m$^3$] | 743.9 |
| IBP | [°C] | 34.6 |
| 20% v/v | [°C] | 55.8 |
| 50% v/v | [°C] | 94.0 |
| FBP | [°C] | 186.3 |
| C | [%wt] | 84.16 |
| H | [%wt] | 13.48 |
| O | [%wt] | 2.36 |
| Paraffins | [vol%] | 43.9 |
| Olefins | [vol%] | 11.7 |
| Naphthenes | [vol%] | 7.8 |
| Aromatics | [vol%] | 26.9 |
| Oxygenates | [vol%] | 7.7 |
| Sulphur | [ppm] | 6 |
| LHV | [MJ/kg] | 42.22 |
| MON | [-] | 85.3 |
| RON | [-] | 96.5 |

mass measurement. The dimensions of the crucible are 7 mm in diameter and 2 mm in height with a soot layer thickness less than 0.1 mm. The experimental procedure started with an initial soot sample conditioned at 40°C during 10 min in an inert atmosphere ($N_2$) to set the same ambient temperature for all tests. Next, the volatile organic compound (VOC) content was removed from the soot sample increasing the temperature till 450°C with a constant heating rate of 3°C/min. Finally, the soot sample was cooled down to 150°C prior to the TGA test. This procedure allowed drawing a symmetric process to the VOC removal and increasing the soot oxidation temperature window (Wang et al., 2014). The final step depended on the thermal strategy: in non-isothermal tests the atmosphere was changed to air ($N_2$ + $O_2$) applying a constant heating rate; in isothermal tests the soot sample was heated up until the targeted temperature was attained and then the atmosphere was changed to a $N_2$ + $O_2$ mixture with predefined $O_2$ concentration.

In this work, a matrix of TGA experiments was available to explore the optimum procedure for the determination of the GDI soot kinetic parameters. Firstly, isothermal TGA tests (635−670−750°C) were combined with different $O_2$ concentration (0.25−1.3−16.6%) as a way to

make explicit the influence of the gas reactant. The tested range emulates real working conditions from very small $O_2$ concentration governed by the lambda control (Möller et al., 2009) to high $O_2$ concentration representative of fuel cut off events in which passive filter regeneration is promoted (Giechaskiel et al., 2019). In addition, three additional isothermal TGA experiments were performed with 16.6% in $O_2$ concentration to cover the low temperature range (500 – 525 – 550°C). These last tests are used as initial validation of the proposed reaction rate expression. As a second TGA experiment, heating rate tests were considered to complete the validation. Isothermal tests are appropriate for model development and identification purposes because of the accurate control of the main test boundary, i.e. the gas temperature and hence the soot sample temperature. By contrast, non-isothermal tests are useful to highly stress the proposed reaction rate model because of the influence of the heating rate on the effective oxidation rate as the temperature increases (Rodríguez-Fernández et al., 2011). Three heating rates of 1, 3 and 5°C/min were selected with 16.6% in $O_2$ concentration.

## 3. Reactivity dependence on the soot mass

The soot oxidation profiles were obtained experimentally from the instantaneous soot mass provided by the TGA test. This mass was employed to define the soot conversion fraction, which is defined according to Eq. 1. First, the difference with respect to the initial soot mass in the sample was considered. Next, the result was normalized with respect to the total mass conversion in every test.

$$\alpha = \frac{m_0 - m_s}{m_0 - m_\infty} \tag{1}$$

In Eq. 1, $\alpha$ is the soot conversion fraction, $m_0$ represents the initial mass of soot, $m_s$ is the actual/instantaneous mass of soot at time t and $m_\infty$ stands for the mass of soot at the end of the experiment. This way, the soot conversion fraction is defined ranging from 0 to 1 in all tests.

The experimental soot reaction rate can be expressed as a function of the soot conversion fraction considering its variation as a function of time. Concerning the representation of the results, the soot oxidation rate is also plotted with respect to the soot conversion fraction instead of time. The advantage is that the comparison is done within a common range. This is opposite to time alternative since every test took different duration as a function of the gas temperature and the $O_2$ concentration.

According to the results in Fig. 1, a difference in reaction rate is found as a function of the gas temperature, as expected from the well-known Arrhenius-like behaviour. However, the reaction rate also shows a clear dependence on the soot conversion fraction and the $O_2$ concentration. Therefore, to analyse firstly the dependence on the soot mass, the reaction rate can be expressed as

$$\frac{\partial \alpha}{\partial t} = (1-\alpha)^n K\left(T, X_{O_2}\right) \tag{2}$$

where $n$ represents the soot reaction order and $K$ is the kinetic term dependent on the temperature and the $O_2$ concentration that governs the intrinsic reactivity (Arrhenius expression), mass transfer and adsorption phenomena, as discussed in Section 4. Thus, the procedure to predict the experimental soot oxidation profile consists of imposing the soot conversion fraction equal to 0 in Eq. 2 initially. The resulting reaction rate is integrated within the time-step to obtain the new value of soot conversion fraction after $\Delta t$. Next, this new value is substituted again in Eq. 2 to continue with the prediction of the reaction rate along the test duration.

Since only the soot mass is varied along every test, $n$ and $K$ can be determined as constant values for each experiment. Fig. 2 represents the solution for $n$ and $K$ obtained applying the Levenberg-Marquardt least-square method (Moré, 1977). These results are referred as average solution since they do not depend on the soot conversion fraction. The resulting correlated reaction rate using these values is compared with the experimental data in Fig. 1, where the determination

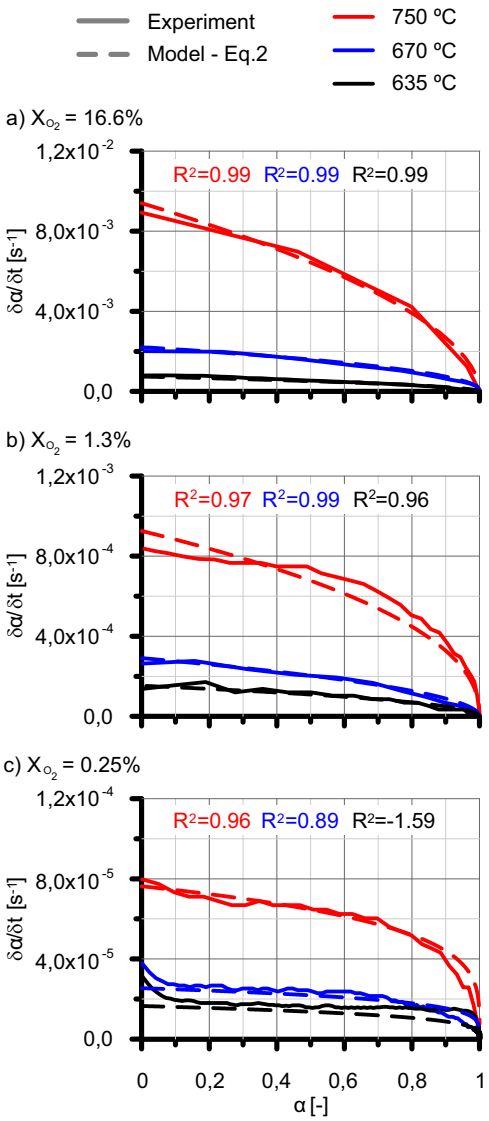


Figure 1: Experimental and modelled soot oxidation rate during isothermal TGA tests.

coefficient $R^2$ is shown. A negative value of the $R^2$ indicates that a constant oxidation rate equal to the mean of the experimental one would provide better prediction, as it happens in the case of 0.25% in $O_2$ concentration at 635°C. The term $K$ will be discussed in Section 4. Fig. 2(a) shows that the soot reaction order is around 0.5 for all tests with the only exception being the very low $O_2$ concentration cases. In these conditions, the soot reaction order falls into the range [0.2-0.3].

An analysis of variance applied to the soot reaction order confirms its sensitivity to the $O_2$ concentration. It is evidenced by means of the p-value, which reaches a level (0.014) below the

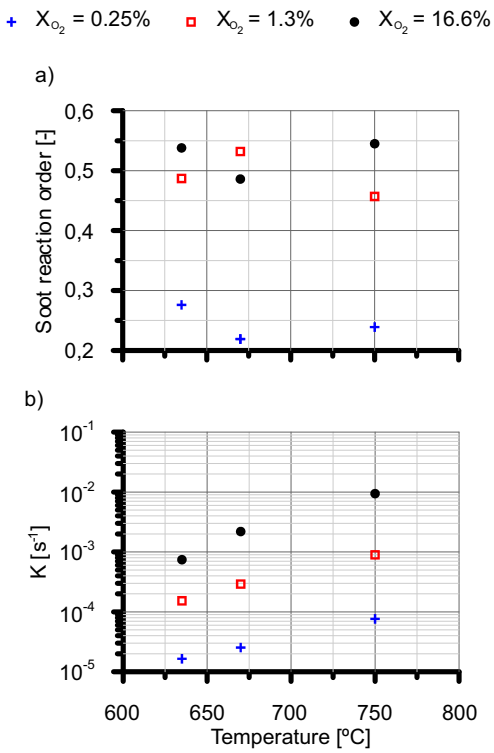


Figure 2: Determination of the average (a) soot reaction order and (b) kinetic term of each TGA test.

significance one (0.05). The p-value is defined as the probability of observing the calculated value if the null hypothesis is true (Ziliak, 2017), so that it helps to distinguish random results from those statistically significative. Besides the influence of the $O_2$ concentration, the instantaneous soot mass also plays a relevant role to fit the optimum instantaneous soot reaction order when the engine operation is close to stoichiometric conditions. Fig. 3(a) represents the instantaneous soot reaction order as a function of the soot conversion fraction for the isothermal TGA tests corresponding to 0.25% in $O_2$ concentration. At the lowest temperature (635°C), the soot reaction order is the lowest one, just slightly over zero. At higher temperature, the soot reaction order has a maximum close to 0.53 till 0.3 in soot conversion fraction. Then it decreases to 0.25 at 0.7 in soot conversion fraction followed by a gradual increase till the completeness of the soot oxidation. This dependence is confirmed by the p-value of the soot conversion fraction, which is represented in Fig. 3(b) for each isothermal TGA test. It does not exceed 0.03 in the tests at very low $O_2$

concentration, i.e. the results present dependence on the soot conversion fraction. However, the p-value falls into the range [0.12-0.16] once the $O_2$ concentration increases over 1%, what reveals the loss of dependence of the reaction rate on the soot mass.

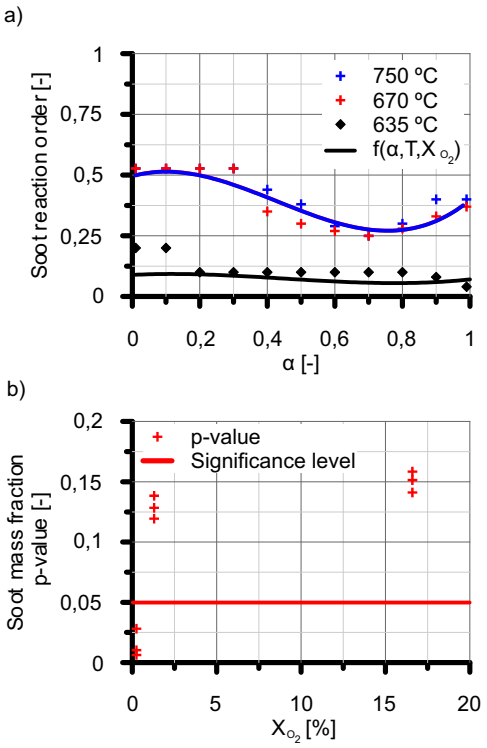


Figure 3: Soot reaction order dependence on the oxidation completeness: (a) soot reaction order as a function of soot conversion fraction and (b) soot conversion fraction p-value.

A phenomenological expression (Eq. 3) is proposed to determine the value of the soot reaction order along the TGA tests once identified its behaviour with respect to the soot conversion fraction and the $O_2$ concentration. The prediction provided by Eq. 3 is represented by the continuous series in Fig. 3(a). A sigmoid term depending on the temperature is included to account for the steep decrease in soot reaction order in the test at 635°C and $X_{O_2} = 0.25\%$. Complementary, Eq. 3 converges to a constant value over this threshold in $O_2$ concentration regardless the soot conversion fraction and the temperature, as observed in the experimental data. Eq. 3 can be applied with confidence to the operating conditions shown in this study. Its application to a wider range of conditions is very useful, particularly from a modelling point of view, to determine the parameters

of the kinetic term with sensitivity to the soot conversion fraction regardless the temperature and the $O_2$ concentration (see Section 4).

$$n = \left(\frac{5,28}{1+e^{776X_{O2}}}\left(2,594\alpha^3 - 3,329\alpha^2 + 0,586\alpha - 0,047\right) + 0,527\right)\left(1 - \frac{0,8501}{1+e^{(X_{O2}T-2.3)(0.277/X_{O2})}}\right) \tag{3}$$

Fig. 4 represents the soot oxidation rate and the re-optimised kinetic term $K$ for every isothermal TGA test obtained from applying Eq. 3. It is compared with the experimental data and the results from using the averaged soot reaction order and kinetic term $K$, which were depicted in Fig. 2. For the sake of clarity, Table 3 specifies the values employed in each model.

Table 3: Models for the determination of the soot oxidation rate in TGA tests as a function of temperature and $O_2$ concentration.

| | | Best fit with $n = cte$ | | Best fit with $n = f(\alpha, T, X_{O_2})$ | |
|---|---|---|---|---|---|
| Temperature [°C] | $X_{O_2}$ [%] | $n$ [-] | $K$ [$s^{-1}$] | $n$ [-] | $K$ [$s^{-1}$] |
| 635°C | 0.25 | 0.106 | $1.65\times10^{-5}$ | Eq. 3 | $1.80\times10^{-5}$ |
| | 1.3 | 0.532 | $1.53\times10^{-4}$ | 0.527 (Eq. 3) | $1.67\times10^{-4}$ |
| | 16.6 | 0.538 | $7.42\times10^{-4}$ | 0.527 (Eq. 3) | $7.92\times10^{-4}$ |
| 670°C | 0.25 | 0.211 | $2.54\times10^{-5}$ | Eq. 3 | $2.97\times10^{-5}$ |
| | 1.3 | 0.525 | $2.91\times10^{-4}$ | 0.527 (Eq. 3) | $2.91\times10^{-4}$ |
| | 16.6 | 0.506 | $2.19\times10^{-3}$ | 0.527 (Eq. 3) | $2.21\times10^{-3}$ |
| 750°C | 0.25 | 0.209 | $7.63\times10^{-5}$ | Eq. 3 | $7.91\times10^{-5}$ |
| | 1.3 | 0.451 | $8.96\times10^{-4}$ | 0.527 (Eq. 3) | $9.08\times10^{-4}$ |
| | 16.6 | 0.589 | $9.41\times10^{-3}$ | 0.527 (Eq. 3) | $9.33\times10^{-3}$ |

As observed in the trend of the coefficient of determination included in Fig. 4, very good agreement is obtained with the experimental data for 1.3% in $O_2$ concentration ($R^2 > 0.94$). In addition, the use of the instantaneous soot reaction order improves the prediction at the lowest $O_2$ concentration (Fig. 4(c)). The benefits are especially relevant as the oxidation is completed leading to the increase of $R^2$ in all cases.

The results represented in Fig. 4 and the convergence of Eq. 3 to 0.527 suggest the use of the cylinder contracting area reaction model for solid-state reactions (Khawam and Flanagan, 2006)

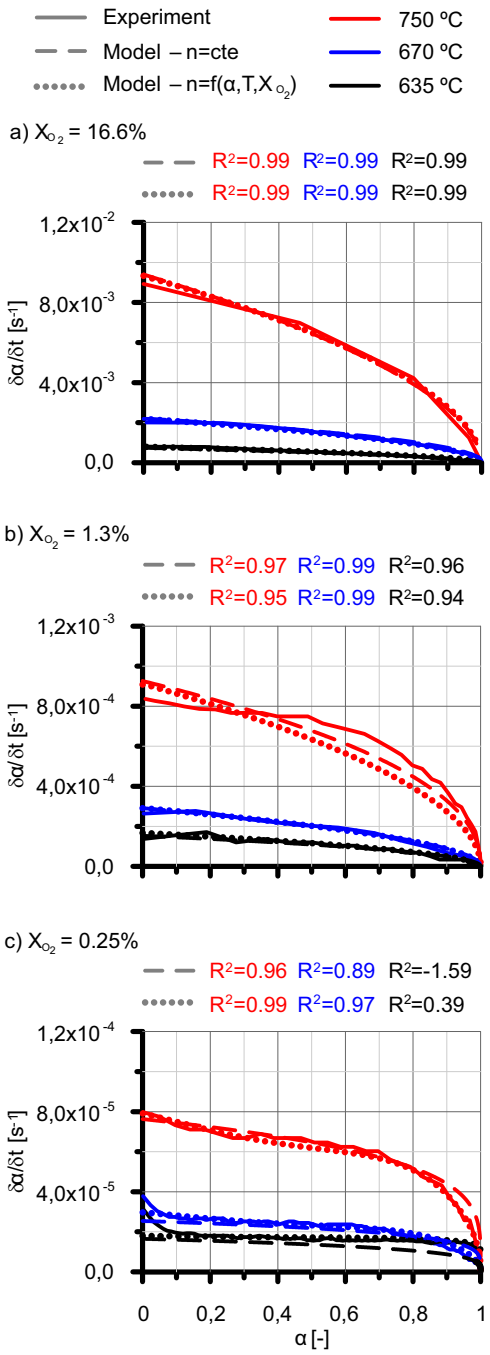


Figure 4: Comparison between experimental soot oxidation rate and prediction from the soot reaction order models.

when the $O_2$ concentration is over 1%. This result for GDI soot agrees with that found for soot from diverse sources, as diesel, hydrotreated vegetable oil (HVO), gas to liquid (GTL) or biodiesel (Sánchez-Valdepeñas, 2018). As described in Eq. 4, this solid-state reaction model is characterised

by a soot reaction order equal to 0.5, so that it becomes an accurate theoretical representation of the soot oxidation process, as also expected according to the results shown in Fig. 2(a). The value of $K\left(T, X_{O_2}\right)$ is modified to $K'\left(T, X_{O_2}\right)$ according to the geometrical constant related to the cylinder contracting area model.

$$\frac{\partial \alpha}{\partial t} = 2\left(1-\alpha\right)^{0.5} K'\left(T, X_{O_2}\right) \tag{4}$$

The cases corresponding to 16.6% and 1.3% in $O_2$ concentration are represented in Fig. 5(a) and (b) respectively. According to the good results provided by this simplification of the soot reaction model, the geometry of the soot aggregates can be said to govern the dynamics of the soot oxidation in $O_2$ excess conditions. It is based on the fact that their averaged fractal dimension is reported within the range [1.44 (LaRocca et al., 2015) - 1.8 (Seong et al., 2013)], i.e. typical of the cylindrical-like structures that define the contracting area model (Khawam and Flanagan, 2006). This feature contrasts with the spherical primary particles that compose the agglomerates, which would be representative of a contracting volume reaction model. Nevertheless, the cylinder contracting area reaction model fails at low $O_2$ concentration because of the soot reaction order variation. This response is clearly observed in Fig. 5(c). In this case, a soot reaction order equal to 0.5 underestimates the oxidation rate. As observed, the temperature window in which the deviation in soot conversion fraction is relevant for the cylinder contracting area model widens as the temperature increases.

## 4. Reactivity dependence on the $O_2$ concentration

Besides the dependence of the soot reaction order on the $O_2$ concentration, the gas reactant has a primary role on the determination of the kinetic term $K$ defined in Eq. 2. Consequently, an accurate determination of the $O_2$ effect on the kinetics is in turn intimately related to the right quantification of the pre-exponential factor and the activation energy of the soot oxidation reaction.

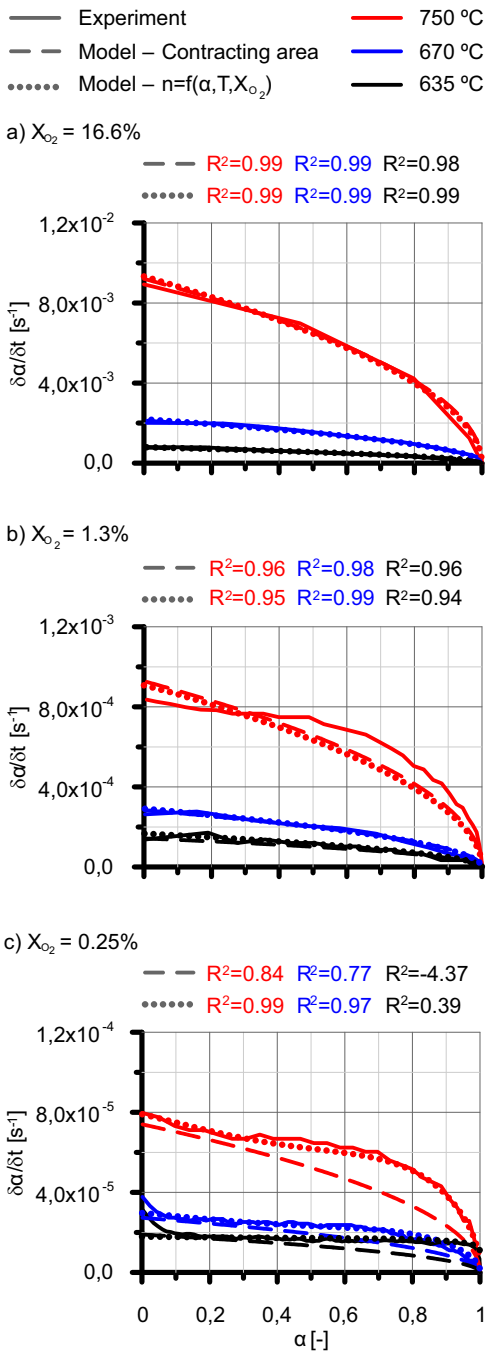


Figure 5: Application of the contracting area reaction model to predict the soot reaction rate in isothermal TGA tests with different $O_2$ concentration.

As usually considered in the literature (Bogarra et al., 2018), constant reaction order with respect to $O_2$ is initially assumed. As a result, the activation energy and the pre-exponential factor

of the Arrhenius expression can be obtained by linearisation of the kinetic term $K$ applying the logarithm method:

$$K = k_{ox} X_{O_2}^r = P_{f_{ox}} e^{-\frac{E_{a_{ox}}}{\Re T}} X_{O_2}^r \tag{5}$$

$$\ln k_{ox} = \ln\left(\frac{K}{X_{O_2}^r}\right) = \ln P_{f_{ox}} - \frac{E_{a_{ox}}}{\Re}\frac{1}{T} \tag{6}$$

Fig. 6 represents the logarithm of the intrinsic kinetic term ($k_{ox}$) as a function of the inverse of the temperature for every TGA test. Applying these data to Eq. 6, the corresponding activation energy and pre-exponential factor for every $O_2$ concentration are summarised in Table 4. The results indicate that the intrinsic kinetic term is linear with temperature provided that the $O_2$ concentration does not vary. This is a misleading result that advises not to rely the soot oxidation characterisation on test campaigns at constant $O_2$ concentration. This approach might lead to be confident on the hypothesis of constant $O_2$ reaction order to determine the activation energy. However, the parametrisation would be only valid for the specific tested $O_2$ concentration but not representative of the regular operation of the regeneration of PFs under real driving conditions. In addition, the variation of the activation energy with temperature at constant $O_2$ concentration also confirms that the $O_2$ reaction order is not constant in actual conditions. Consequently, the oxygen adsorption must be considered as a governing process of the reaction dynamics. Its influence can be described by means of an isotherm based reaction rate, whose use is equivalent to a variable reaction order that depends on temperature and $O_2$ concentration, as discussed by Macián et al. (2019). Therefore, the use of the Langmuir (LG) and Dubinin-Radushkevich (DR) isotherms is proposed to explore the dependence of the soot oxidation on the $O_2$ concentration.

Firstly, the efficiencies of the various mass transfer processes that can take place in a TGA experiment have been considered to assess their effect on the soot oxidation rate and on the determination of the intrinsic kinetic parameters. For this purpose, the proposal of Song et al. (2006)

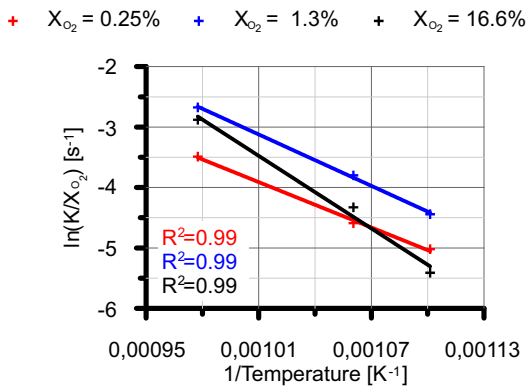


Figure 6: Dependence of the soot oxidation intrinsic kinetic term on temperature and $O_2$ concentration.

Table 4: Pre-exponential factor and activation energy of the soot oxidation as a function of the $O_2$ concentration assuming $O_2$ first-order kinetics.

| $X_{O_2}$ [%] | $P_{f_{ox}}$ [s$^{-1}$] | $E_{a_{ox}}$ [J/mol] |
|---|---|---|
| 0.25 | $6.21\times10^{3}$ | 103917 |
| 1.3 | $7.25\times10^{5}$ | 117826 |
| 16.6 | $1.86\times10^{8}$ | 166405 |

was applied to calculate the intraparticle, interparticle and external diffusion efficiencies. Since the TGA experiments were carried out under isothermal conditions, the heat transfer processes were assumed negligible, as commonly done in the literature in these cases (Jaramillo et al., 2014).

The intraparticle diffusion efficiency is calculated as a function of the Thiele modulus referred to the spherical soot particles as

$$\eta_p = \frac{3}{\varphi_p}\left(\frac{1}{\tanh\varphi_p} - \frac{1}{\varphi_p}\right), \tag{7}$$

where $\eta_p$ is the intraparticle diffusion efficiency and $\varphi_p$ represents the Thiele modulus calculated using the GDI soot geometric properties given by Choi et al. (2015).

Similarly, the interparticle diffusion is related to the mass transfer throughout the soot sample layer. If the soot sample behaves like a flat plate, the interparticle diffusion efficiency is given by the Thiele modulus referred to the layer thickness as

$$\eta_l = \frac{1}{\tanh \varphi_l}. \tag{8}$$

Finally, the external diffusion, which defines the mass transfer from the bulk gas to the external surface of the soot sample, is calculated from the $O_2$ molecular diffusivity and the maximum oxidation rate corrected by the intraparticle and interparticle diffusion efficiencies according to (Song et al., 2006):

$$\frac{1-\eta_e}{\eta_e} = \frac{\eta_p \eta_l K_{max} \nu_{O_2} e\,(L-e)}{D_{m_{O_2}}} \tag{9}$$

The efficiency of every diffusion step is represented in Fig. 7 as a function of temperature and $O_2$ concentration being indicated the particular result for the isothermal TGA tests. The effective diffusion efficiency, i.e. the product of the three contributions, is represented for $X_{O_2} = 0.25\%$, since this is the most restrictive condition. The results are similar to those provided by Song et al. (2006). The main diffusion limitations are given by the external and interparticle mass transfer as the temperature increases. Nevertheless, the diffusion is not highly affecting the oxidation rate, being the effective diffusion efficiency over 0.92 in all cases.

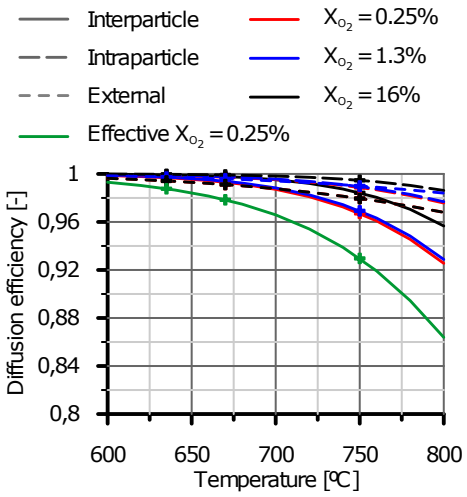


Figure 7: Diffusion efficiency of every mass transfer step in the isothermal TGA tests.

Taking into account the mass transfer contribution, if the Langmuir isotherm (Langmuir, 1948) is applied, the kinetic term is expressed as

$$K_{LG} = \eta_e \eta_p \eta_l k_{ox} \frac{K_S X_{O_2}}{K_S X_{O_2} + 1}, \tag{10}$$

where $K_S$ is the adsorption equilibrium constant obtained according to Eq. 11:

$$\left.\begin{aligned} k_{ads} &= P_{f_{ads}} e^{-\frac{Ea_{ads}}{\Re T}} \\ k_{des} &= P_{f_{des}} e^{-\frac{Ea_{des}}{\Re T}} \end{aligned}\right\} K_S = \frac{P_{f_{ads}}}{P_{f_{des}}} e^{-\frac{Ea_{ads} - Ea_{des}}{\Re T}} = P_{f_S} e^{-\frac{\Delta H_S}{\Re T}} \tag{11}$$

In Eq. 11, $\Delta H_S$ is the adsorption enthalpy, which is defined as the adsorption to desorption activation energy difference, and $P_{f_S}$ represents the pre-exponential factor of the sorption process.

The Langmuir isotherm has provided good results to model the dynamics of the diesel soot oxidation in the presence of $NO_2$ (Messerer et al., 2006) and $O_2$ (Macián et al., 2019). The main reason is the further sensitivity to the temperature brought to the reaction rate expression by the gaseous reactant adsorption limitations. However, the Langmuir isotherm was evaluated with experimental data obtained with constant gaseous reactant concentration. Due to the uncertainty on the Langmuir isotherm capability in tests with different concentration in gaseous reactant, the Dubinin-Radushkevich isotherm is also considered to complete the analysis. Opposite to the Langmuir model, the Dubinin-Radushkevich isotherm (Dubinin and Radushkevich, 1947) assumes heterogeneous surface and multi-layer adsorption involving Van Der Waals forces. The model equation is semi-empirical and describes the pore filling based on a change in the potential energy between the gas and adsorbed phases and a characteristic energy of a given solid (Nguyen and Do, 2001). It is applied to describe the adsorption in microporous substrates, with good results in carbonaceous materials (Nguyen and Do, 2001). Eq. 12 defines the kinetic term K according to the Dubinin-Radushkevich model,

$$K_{DR} = \eta_e \eta_p \eta_l k_{ox} e^{-\beta \varepsilon^2}, \tag{12}$$

where $\beta$ is a constant and $\varepsilon$ is the Polany potential calculated as:

$$\varepsilon = \Re T \ln\left(1 + \frac{1}{X_{O_2}}\right) \tag{13}$$

The parameters of the Langmuir and Dubinin-Radushkevich isotherms, as well as the oxidation pre-exponential factor and activation energy, were determined applying the Levenberg-Marquardt method. The kinetic terms corresponding to the case $n = f(\alpha, T, X_{O_2})$ of each isothermal TGA experiment detailed in Table 3 were considered in this calibration procedure. The value of the parameters and the predicted kinetic terms can be found in Table 5 and Fig. 8, respectively. Although this calibration is affected by the operating conditions in which the soot was collected, the order of magnitude of the activation energy falls into the range found in previous works for gasoline soot (Bogarra et al., 2016). At the same time, the proposed procedure provides good accuracy to determine the pre-exponential factor since the soot reaction order, the $O_2$ adsorption and the mass transfer limitations are considered.

Langmuir and Dubinin-Radushkevich isotherms provide similar activation energy ($\pm 160$ kJ/mol). However, the greater consistency of the Dubinin-Radushkevich model within the entire temperature and $O_2$ concentration ranges is clearly observed in Fig. 8(b). Its deviation with respect to the kinetic term obtained from the experiments assuming $n = f(\alpha, T, X_{O_2})$ (Table 3) is always lower than the one provided by the Langmuir isotherm. In fact, the Langmuir isotherm only works at high $O_2$ concentration, in agreement with the results obtained by Macián et al. (2019) in PF active regenerations. However, the Langmuir model completely fails close to stoichiometric conditions, being just able to capture the dependence on temperature of the kinetic term (Fig. 8(a)).

The predicted soot oxidation rate along the isothermal TGA tests is shown in Figs. 9 and 10 applying the kinetic terms obtained with Langmuir and Dubinin-Radushkevich models, respectively. These models are combined with the soot reaction order obtained using Eq. 3. An overall comparison leads to conclude that the Dubinin-Radushkevich model behaves better than the Langmuir

Table 5: Parameters of the kinetic term $K$ for the Langmuir and Dubinin-Radushkevich models.

| | | Langmuir | Dubinin-Radushkevich |
|---|---|---|---|
| $P_{f_{ox}}$ | [$s^{-1}$] | $3.37\times10^{6}$ | $2.65\times10^{6}$ |
| $E_{a_{ox}}$ | [J/mol] | 162600 | 160400 |
| $P_{f_S}$ | [-] | 0.00267 | |
| $\Delta H_S$ | [J/mol] | -64252 | |
| $\beta$ | [$mol^2/J^2$] | | $2.09\times10^{-9}$ |

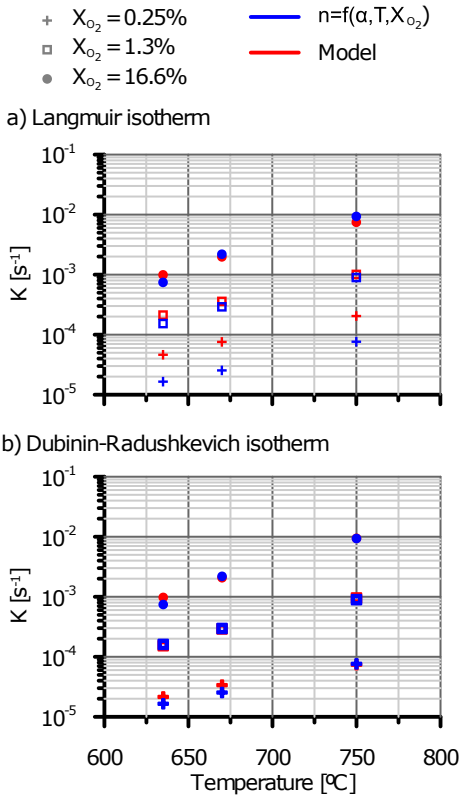


Figure 8: Comparison of the experimental kinetic term $K$ with (a) Langmuir and (b) Dubinin-Radushkevich models.

approach. Both models perform very similar at the highest $O_2$ concentration with the only exception of the highest temperature test, where the Langmuir model underestimates the oxidation rate. The Dubinin-Radushkevich model is fully consistent at $X_{O_2} = 1.3\%$. By contrast, the reaction rate predicted by the Langmuir model diverges as the temperature decreases. The largest differences appear in the TGA tests at $X_{O_2} = 0.25\%$. Under this atmosphere, the Langmuir model is unable to capture the oxidation dynamics and overestimates the reaction rate. Conversely, the soot oxi-

dation rate predicted by the Dubinin-Radushkevich isotherm is more precise. Only at the lowest temperature the Dubinin-Radushkevich model provides a negative coefficient of determination, as happens with the Langmuir model at all temperatures. Despite this case conditioned by the low standard deviation of the experimental data, the Dubinin-Radushkevich model can be concluded to provide an accurate quantitative prediction within the tested range.

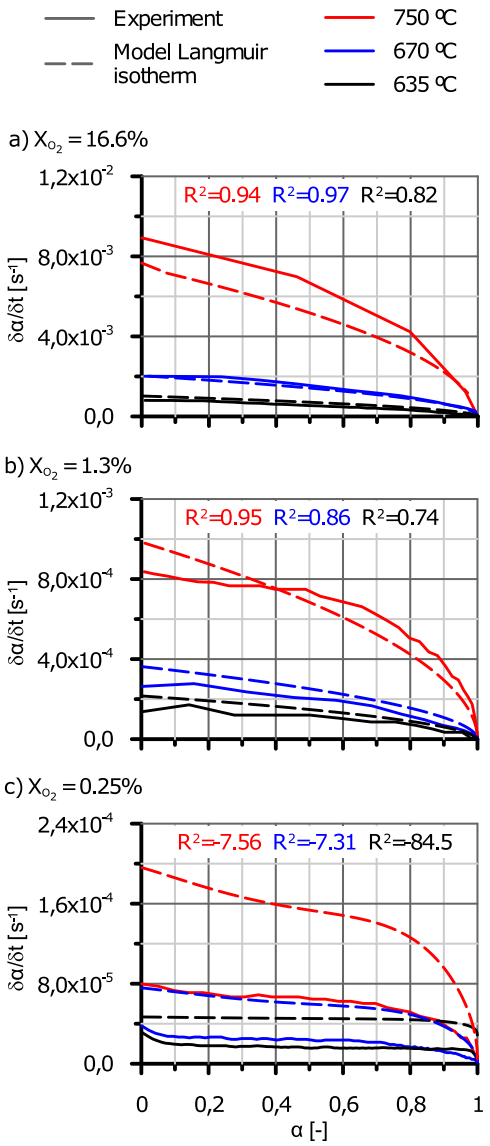


Figure 9: Comparison of the experimental soot oxidation rate with the prediction of the Langmuir model in isothermal TGA tests at different temperature and $O_2$ concentration.

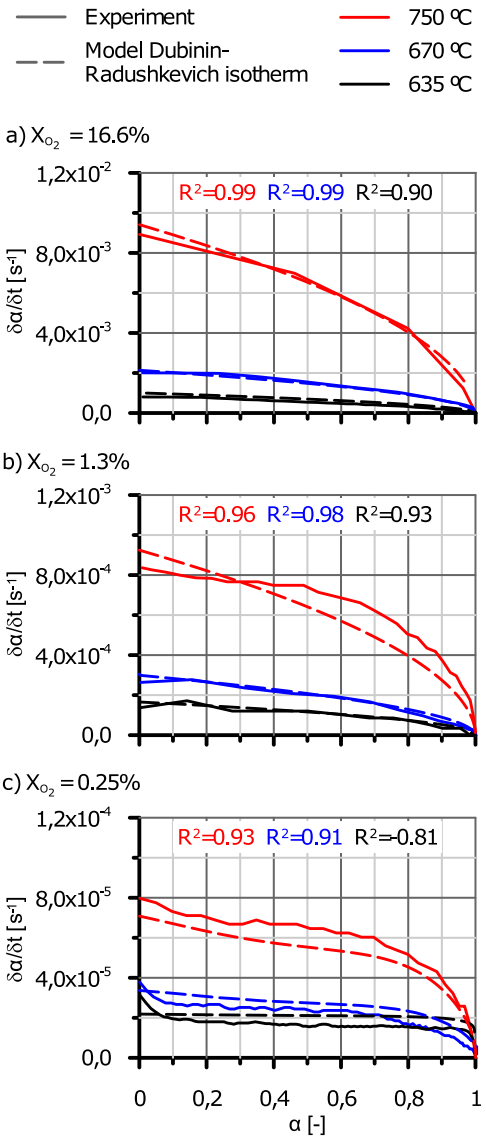


Figure 10: Comparison of the experimental soot oxidation rate with the prediction of the Dubinin-Radushkevich model in isothermal TGA tests at different temperature and $O_2$ concentration.

The capability of the model combining the calculation of the instantaneous soot reaction order and the Dubinin-Radushkevich isotherm is examined against additional TGA tests non-used in the calibration. The results obtained applying the Langmuir isotherm are also considered for the sake of completeness.

Three low temperature isothermal TGA tests are represented in Fig. 11 covering the range from 500 to 550°C with 16.6% in $O_2$ concentration. In agreement with the results shown in

plot (a) of Figs. 9 and 10, both models behave similar at this $O_2$ concentration. However, the Dubinin-Radushkevich isotherm yields more accurate results and only slightly overpredicts the soot depletion rate at 550°C. In comparison, the Langmuir model shows larger deviation at this temperature, although its ability to predict the trends in oxidation rate is still acceptable.

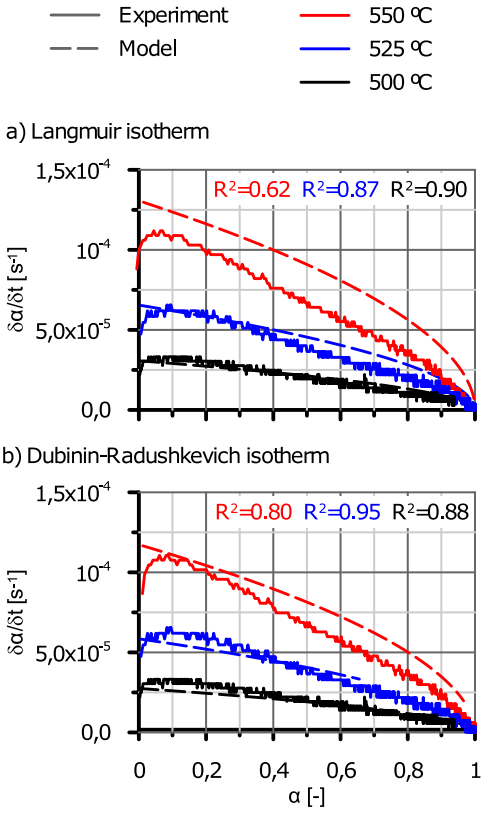


Figure 11: Comparison of the experimental soot oxidation rate with the prediction of the Langmuir and Dubinin-Radushkevich models in isothermal TGA tests at low temperature with 16.6% in $O_2$ concentration.

The validation of the proposed model is completed using non-isothermal TGA tests, which are represented in Fig. 12. The heating rate was constant during every test, ranging from 1°C/min to 5°C/min; the $O_2$ concentration was kept at 16.6% in all tests. The Langmuir (Fig. 12(a)) and the Dubinin-Radushkevich (Fig. 12(b)) models provide very similar results in terms of oxidation dynamics, as shown in Fig. 12, and characteristic parameters, which are summarised in Table 6. These results confirm that both models behave similar under $O_2$ excess conditions.

In particular, the starting oxidation temperature (SOT), which is defined as the temperature at which the soot conversion fraction reaches 5%, and the maximum mass loss rate temperature (MMLRT) (Rodríguez-Fernández et al., 2016) are detailed in Table 6. Both models capture the experimental SOT and MMLRT properly, despite the noisy experimental signal (Bogarra et al., 2016). Nevertheless, the predicted SOT is greater than the experimental one in all cases. Opposite, the calculated MMLRT is closer to the experimental value, both below and above. According to these trends in SOT and MMLRT, the modelled oxidation rate is slightly larger than the experimental one between these two characteristic temperatures due to mass conservation. This happens at every heating rate but becomes more evident at test with 1°C/min in heating rate. Nevertheless, the maximum oxidation rate is also determined with good accuracy, as observed in Fig. 12.

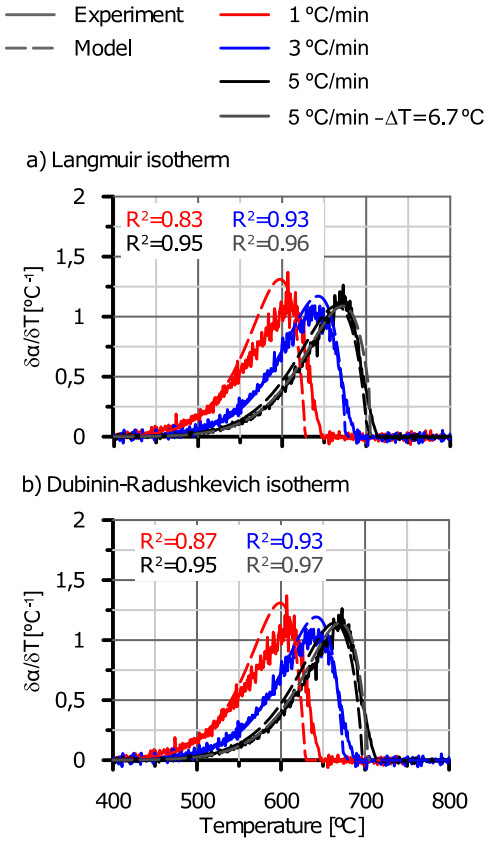


Figure 12: Comparison of the experimental soot oxidation rate with the prediction of the Langmuir and Dubinin-Radushkevich models in non-isothermal TGA tests with different heating rate and 16.6% in $O_2$ concentration.

Table 6: Comparison of SOT and MMLRT between experimental data, Langmuir model and Dubinin-Radushkevich model in non-isothermal TGA tests with different heating rate and 16.6% in $O_2$ concentration.

| | SOT [°C] | | | MMLRT [°C] | | |
|---|---|---|---|---|---|---|
| | Experiment | LG | DR | Experiment | LG | DR |
| 1 °C/min | 500 | 501 | 500.7 | 604.8 | 596.3 | 597.7 |
| 3 °C/min | 528.8 | 536 | 536 | 638.8 | 642 | 642 |
| 5 °C/min | 541.7 | 553.3 | 553.3 | 672.7 | 665 | 663.3 |
| 5 °C/min ($\Delta$T = 6.7°C) | 541.7 | 560 | 560 | 672.7 | 671.7 | 670 |

Finally, it is worth to note that the model prediction of the case corresponding to 5°C/min in heating rate presents a shift of the oxidation rate regardless the model approach. In fact, the modelled results should be delayed 6.7°C/min to increase the accuracy in the temperature region between SOT and MMLRT, as evidenced in Fig. 12 (grey series). Since the proposed model is sensitive to the change of the experimental response between 1°C/min and 3°C/min in heating rate, the shift appearing at 5°C/min can be attributed to higher dependence on the heat transfer phenomena, which have been neglected in this work. According to the results, the well-known SOT and MMLRT increase as the heating rate does due to the lower dwell time for oxidation at a given temperature is aggravated by thermal inertia effects. Consequently, a temperature gradient between the gas and the soot sample appears and reduces the expected oxidation rate (model prediction) below the MMLRT, i.e. the experimental reaction rate is lower than the modelled one when thermal inertia is neglected at high heating rates. In view of these results, the heating rate should be kept below 5°C/min to avoid the negative impact of heat transfer on the determination of the soot kinetic parameters in non-isothermal TGA tests.

## 5. Summary and conclusions

A detailed analysis of the GDI soot oxidation reactivity has been presented applying a novel experimental-theoretical methodology. The experimental procedure consists of isothermal TGA tests performed with different $O_2$ concentration. The testing matrix covers representative ranges

for all the involved parameters (temperature, gaseous reactant concentration and soot conversion fraction) in soot regeneration under realistic driving operation conditions.

The analysis of the results has shown the benefits of decoupling the contribution of the solid-state model from the kinetic term, which depends mainly on the temperature and the concentration of the gaseous reactant. The soot reaction order has been proved to be properly represented by the cylinder contracting area model, i.e. soot reaction order equal to 0.5, when the $O_2$ concentration is over 1.3%. From the engine point of view, this soot reaction order results suitable for GPF regeneration modelling during fuel cut-off phases. However, the average soot reaction order of the TGA test decreases to 0.2-0.3 when the $O_2$ concentration is 0.25%, which represents the concentration during the lean combustion phase imposed by the engine lambda control. For these operating conditions, the cylinder contracting area model fails. In addition, the analysis of the instantaneous soot reaction order along the oxidation process reveals a marked sensitivity to the completeness of the reaction as well as the appearance of temperature dependence.

In parallel, the kinetic term has been examined in detail. A modelling approach based on the Arrhenius expression with constant $O_2$ reaction order has been evidenced to be erroneous because of the dependence of the activation energy on the $O_2$ concentration and the temperature. This result underlines the need to account for the limitations that the mass transfer and oxygen adsorption impose to the soot oxidation rate. In this regard, the Langmuir and the Dubinin-Radushkevich isotherms have been evaluated. Although both models provide similar accuracy when $O_2$ is available in excess, the Dubinin-Radushkevich isotherm has also shown the ability to capture the oxidation dynamics in cases with very low $O_2$ concentration. Therefore, the adsorption-based Dubinin-Radushkevich model should be employed to represent the soot oxidation within the entire GPF operation window under real driving conditions.

## Acknowledgements

This research has been partially supported by FEDER and the Government of Spain through project TRA2016-79185-R.

## References

[1] 2007. 715/2007 of the European Parliament and of the Council on type-approval of motor vehicles with respect to emissions from light passenger and commercial vehicles (Euro 5 and Euro 6) and on access to vehicle repair and maintenance information. Official Journal of the European Union.

[2] Alkidas, A.C., 2007. Combustion advancements in gasoline engines. Energy Convers. Manag. 48, 2751-2761.

[3] Bahreini, R., Xue, J., Johnson, K., Durbin, T., Quiros, D., Hu, S., Huai, T., Ayala, A., Jung, H., 2015. Characterizing emissions and optical properties of particulate matter from PFI and GDI light-duty gasoline vehicles. J. Aerosol Sci. 90, 144–153.

[4] Belot, I., Vidal, D., Votsmeier, M., Hayes, R.E., Bertrand, F., 2020. Numerical investigation of the impact of washcoat distribution on the filtration performance of gasoline particulate filters Chem. Eng. Sci. 221, 115656.

[5] Bogarra, M., Herreros, J.M., Tsolakis, A., York, A.P.E., Millington, P.J., 2016. Study of particulate matter and gaseous emissions in gasoline direct injection engine using on-board exhaust gas fuel reforming. Appl. Energy 180, 245–255.

[6] Bogarra, M., Herreros, J.M., Tsolakis, A., York, A.P.E., Millington, P.J., Martos, F.J., 2017. Influence of on-board produced hydrogen and three way catalyst on soot nanostructure in Gasoline Direct Injection engines. Carbon 120, 326–336.

[7] Bogarra, M., Herreros, J.M., Tsolakis, A., York, A.P.E., Millington, P.J., Martos, F.J., 2017. Impact of exhaust gas fuel reforming and exhaust gas recirculation on particulate matter morphology in Gasoline Direct Injection Engine. J. Aerosol Sci. 103, 1–14.

[8] Bogarra, M., Herreros, J.M., Tsolakis, A., Rodríguez-Fernández, J., York, A.P.E., Millington, P.J., 2018. Gasoline direct injection engine soot oxidation: Fundamentals and determination of kinetic parameters. Combust. Flame 19, 177–187.

[9] Charron, A., Harrison, R.M., Quincey, P., 2007. What are the sources and conditions responsible for exceedances of the 24 h PM10 limit value (50 $\mu gm^{-3}$) at a heavily trafficked London site?. Atmos. Environ. 41, 960–975.

[10] Choi, S., Seong, H., 2015. Oxidation characteristics of gasoline direct-injection (GDI) engine soot: Catalytic effects of ash and modified kinetic correlation. Combust. Flame 162, 2371–2389.

[11] Deng, Y., Zheng, W., Jiaqiang, E., Zhang, B., Zhao, X., Zuo, Q., Zhang, Z., Han, D., 2017. Influence of geometric characteristics of a diesel particulate filter on its behavior in equilibrium state. Appl. Therm. Eng. 123, 61–73.

[12] Dubinin, M.M., Radushkevich, L.V., 1947. The equation of the characteristic curve of activated charcoal. Proc. USSR Acad. Sci. 55, 331–337.

[13] Ess, M.N., Bladt, H., Mühlbauer, W., Seher, S.I., Züllner, C., Lorenz, S., Brüggemann, D., Nieken, U., Ivleva, N.P., Niessner, R., 2016. Reactivity and structure of soot generated at varying biofuel content and engine operating parameters. Combust. Flame 163, 157–169.

[14] Fan, C., Song, C., Lv, G., Wei, J., Zhang, X., Qiao, Y., Liu, Y., 2019. Impact of post-injection strategy on the physicochemical properties and reactivity of diesel in-cylinder soot. Proc. Combust. Inst. 37(4), 4821–4829.

[15] Feng, W., Li, H., Wang, S., Van Halm-Lutterodt, N., An, J., Liu, Y., Liu, M., Wang, X., Guo, X., 2019. Short-term PM10 and emergency department admissions for selective cardiovascular and respiratory diseases in Beijing, China. Sci. Total Environ. 657, 213–221.

[16] Gaddam, C.K., Vander Wal, R.L., 2013. Physical and chemical characterization of SIDI engine particulates. Combust. Flame 160, 2517–2528.

[17] Giechaskiel, B., Joshi, A., Ntziachristos, L., Dilara, P., 2019. European regulatory framework and particulate matter emissions of gasoline light-duty vehicles: a review. Catalysts 9, 586–616.

[18] Hurt, R.H., Haynes, B.S., 2005. On the origin of power-law kinetics in carbon oxidation. Proc. Combust. Inst. 30, 2161–2168.

[19] Jaramillo, I.C., Gaddam, C.K., Vander Wal, R.L., Huang, C., Levinthal, J.D., Lighty, J.S., 2014. Soot oxidation kinetics under pressurized conditions. Combust. Flame 161, 2951-2965.

[20] Jaramillo, I.C., Gaddam, C.K., Vander Wal, R.L., Lighty, J.S., 2015. Effect of nanostructure oxidative pressure and extent of oxidation on model carbon reactivity. Combust. Flame 165, 1848–1856.

[21] Jian, S., Yang, Y., Ren, W., Xing, L., Zhao, D., Tian, Y., Ding, T., Li, X., 2020. Kinetic analysis of morphologies and crystal planes of nanostructured CeO2 catalysts on soot oxidation. Chem. Eng. Sci. 226, 115891.

[22] Jiaqiang, E., Pham, M., Deng, Y., Nguyen, T., Duy, V., Le, D., Zuo, W., Peng, Q., Zhang, Z., 2018. Effects of injection timing and injection pressure on performance and exhaust emissions of a common rail diesel engine fueled by various concentrations of fish-oil biodiesel blends. Energy 149, 979–989.

[23] Joshi, A., 2019. Review of vehicle engine efficiency and emissions. SAE Int. J. Adv. & Curr. Prac. in Mobility 1, 734–761.

[24] Khawam, A., Flanagan, D.R., 2006. Solid-state kinetic models: basics and mathematical fundamentals. J. Phys. Chem. B 35, 17315–17328.

[25] Kong, X., Li, Z., Shen, B., Wu, Y., Zhang, Y., Cai, D., 2019. Simulation of flow and soot particle distribution in wall-flow DPF based on lattice Boltzmann method. Chem. Eng. Sci. 202, 169–185.

[26] Langmuir, I., 1948. The production of rain by a chain reaction in Cumulus clouds of temperatures above freezing. J. Met. 5, 175–192.

[27] Lapuerta, M., Rodríguez-Fernández, J., Sánchez-Valdepeñas, J., 2020. Soot reactivity analysis and implications on diesel filter regeneration. Progr. Energ. Combust. 78, 100833.

[28] La Rocca, A., Bonatesta, F., Fay, M.W., Campanella, F., 2015. Characterisation of soot in oil from a gasoline direct injection engine using Transmission Electron Microscopy. Tribol. Int. 86, 77–84.

[29] Lee, K.O., Seong, H., Choi, S.M., 2013. Detailed analysis of kinetic reactions in soot oxidation by simulated diesel exhaust emissions. Proc. Combust. Inst. 34(2), 3057–3065.

[30] Luo, Y., Zhu, L., Fang, J., Zhuang, C., Guan, C., Xia, C., Xie, X., Huang, Z., 2015. Size distribution chemical composition and oxidation reactivity of particulate matter from gasoline direct injection (GDI) engine fueled with ethanol-gasoline fuel. Appl. Therm. Eng. 89, 647–655.

[31] Macián, V., Serrano, J.R., Piqueras, P., Sanchis, E.J., 2019. Internal pore diffusion and adsorption impact on the soot oxidation in wall-flow particulate filters. Energy 179, 407–421.

[32] Manousakas, M, Bairachtari, K., Kantarelou, V., Eleftheriadis, K., Vasilakos, C., Assimakopoulos, V.D., Maggos, T., 2019. The traffic signature on the vertical PM profile: Environmental and health risks within an urban roadside environment. Sci. Total Environ. 646, 448–459.

[33] Maricq, M.M., Szente, J.J., Jahr, K., 2012. The impact of ethanol fuel blends on PM emissions from a light-duty GDI vehicle. Aerosol Sci. Tech. 46, 576–583.

[34] Messerer, A., Niessner, H., Pöschi, U., 2006. Comprehensive kinetic characterization of the oxidation and gasification of model and real diesel soot by nitrogen oxides and oxygen under engine exhaust conditions: Measurement Langmuir-Hinshelwood and Arrhenius parameters. Carbon 44, 307–324.

[35] Moré, J.J., 1977. The Levenberg-Marquardt algorithm: implementation and theory Numerical Analysis - Lecture Notes in Mathematics. Springer, Verlag.

[36] Möller, R., Votsmeier, M., Onder, C., Guzzella, L., Gieshoff, J., 2009. Is oxygen storage in three-way catalysts an equilibrium controlled process?. Appl. Catal. B 91, 30–38.

[37] Nguyen, C., Do, D.D., 2001. The Dubinin-Radushkevich equation and the underlying microscopic adsorption description. Carbon 39, 1327–1336.

[38] Payri, F., Broatch, A., Serrano, J.R., Piqueras, P., 2011. Experimental-theoretical methodology for determination of inertial pressure drop distribution and pore structure properties in wall-flow diesel particulate filters (DPFs). Energy 36, 6731–6744.

[39] Pfau, S.A., La Rocca, A., Haffner-Staton, E., Rance, G.A., Fay, K., Brough, R.J., Malizia, S., 2018. Comparative nanostructure analysis of gasoline turbocharged direct injection and diesel soot-in-oil with carbon black. Carbon 139, 342–352.

[40] Rodríguez-Fernández, J., Oliva, F., Vázquez, R.A., 2011. Characterization of the diesel soot oxidation process through an optimized thermogravimetric method. Energy Fuels 25, 2039–2048.

[41] Rodríguez-Fernández, J., Hernández, J.J., Sánchez-Valdepeñas, J., 2016. Effect of oxygenated and paraffinic alternative diesel fuels on soot reactivity and implications on DPF regeneration. Fuel 185, 460–467.

[42] Rubino, L., Thier, D., Schumann, T., Guettler, S., Russ, G., 2017. Fundamental study of GPF performance on soot and ash accumulation over Artemis urban and motorway cycles-comparison of engine bench results with GPF durability study on road.in: SAE Technical Paper 2017-24-0127.

[43] Sánchez-Jiménez, P.E., Criado, J.M., Pérez-Maqueda, L.A., 2008. Kissinger kinetic analysis of data obtained under different heating schedules. J. Therm. Anal. Calorim. 94, 427–432..

[44] Sánchez-Valdepeñas, J., 2018. Soot characterization and implications on its reactivity in diesel particulate filters. Ph.D. Thesis (text in Spanish), Universidad de Castilla la Mancha.

[45] Seong, H., Lee, K., Cho, S., 2013. Effects of engine operating parameters on morphology of particulates from a gasoline direct injection (GDI) engine, in: SAE Technical Paper 2013-01-2574.

[46] Serrano, J.R., Climent, H., Piqueras, P., Angiolini, E., 2016. Filtration modelling in wall-flow particulate filters of low soot penetration thickness. Energy 112, 883–898.

[47] Singh, V., Biswal, A., Kesarkar, A.P., Mor, S., Ravindra, K., 2020. High resolution vehicular PM10 emissions over megacity Delhi: Relative contributions of exhaust and non-exhaust sources. Sci. Total Environ. 699, 134273.

[48] Song, Q., He, B., Yao, Q., Meng, Z., Chen, Z., 2006. Influence of diffusion on thermogravimetric analysis of carbon black oxidation. Energ. Fuel. 20, 1895–1900.

[49] Soriano, J.A., Agudelo, J.R., López, A.F., Armas, O., 2017. Oxidation reactivity and nanostructural characterization of the soot coming from farnesane-A novel diesel fuel derived from sugar cane. Carbon 125, 516–529.

[50] Wang, C., Xu, H., Herreros, J.M., Lattimore, T., Shuai, S., 2014. Fuel effect on particulate matter composition and soot oxidation in a direct-injection spark ignition (DISI) engine. Energy Fuels 28, 2003–2012.

[51] Wang, X., Li, S., Adeosun, A., Li, Y., Vujanović, M., Tann, H., Duić, N., 2017. Effect of potassium-doping and oxygen concentration on soot oxidation in O2/CO2 atmosphere: A kinetics study by thermogravimetric analysis. Energy Convers. Manag. 149, 686–697.

[52] Wang-Hansen, C., Ericsson, P., Lundberg, B., Skoglundh, M., Carlsson, P.A., Andersson, B., 2013. Characterization of particulate matter from direct injected gasoline engines. Top. Catal. 56, 446–451.

[53] Zhang, B., Jiaqiang, E., Gong, J., Yuan, W., Zhao, X., Hu, W., 2017. Influence of structural and operating factors on performance degradation of the diesel particulate filter based on composite regeneration. Appl. Therm. Eng. 121, 838–852.

[54] Zhang, M., Hong, W., Xie, F., Su, Y., Liu, H., Zhou, S., 2018. Combustion, performance and particulate matter emissions analysis of operating parameters on a GDI engine by traditional experimental investigation and Taguchi method. Energy Convers. Manag. 164, 344–352.

[55] Ziliak, S., 2017. P-values and the search for significance. Nat. Methods 14, 3–4.

[56] Zimmerman, N., Wang, J.M., Jeong, C., Ramos, M., Hilker, N., Healy, R.M., Sabaliauskas, K., Wallace, J.S., Evans, G.J., 2016. Field measurements of gasoline direct injection emission factors: spatial and seasonal variability. Environ. Sci. Technol. 5, 2035–2043.

## Nomenclature

| | |
|---|---|
| $D_{m_{O_2}}$ | molecular diffusivity |
| $e$ | thickness of the particle layer |
| $E_a$ | activation energy |
| $H_S$ | adsorption enthalpy |
| $k$ | intrinsic kinetic term |
| $K$ | kinetic term |
| $K$ | kinetic term |
| $K'$ | kinetic term for contracting area approach |
| $K_{DR}$ | kinetic term using Dubinin-Radushkevich isotherm model |
| $K_{LG}$ | kinetic term using Langmuir isotherm model |

| | |
|---|---|
| $K_{max}$ | kinetic term without mass transfer limitation |
| $K_S$ | adsorption constant |
| $L$ | height of crucible |
| $m_0$ | initial sample mass |
| $m_\infty$ | sample mass at the end of test |
| $m_s$ | sample mass |
| $n$ | soot reaction order |
| $P_f$ | pre-exponential factor |
| $r$ | $O_2$ reaction order |
| $\mathfrak{R}$ | gas constant |
| $t$ | time |
| $T$ | temperature |
| $X_{O_2}$ | $O_2$ molar concentration |

Greek letters

| | |
|---|---|
| $\alpha$ | soot conversion fraction |
| $\beta$ | Dubinin-Radushkevich adsorption constant |
| $\Delta$ | variation |
| $\varepsilon$ | Polany potential |
| $\varphi$ | Thiele modulus |
| $\eta$ | Diffusion efficiency |
| $\nu_{O_2}$ | $O_2$ stoichiometric factor |

Acronyms

| | |
|---|---|
| DR | Dubinin-Radushkevich |

| | |
|---|---|
| GDI | gasoline direct injection |
| GPF | gasoline particulate filter |
| GTL | gas to liquid |
| HVO | hydrotreated vegetable oil |
| IBP | initial boiling point |
| IMEP | indicated mean effective pressure |
| FBP | final boiling point |
| LG | Langmuir |
| LHV | lower heating value |
| MMLRT | maximum mass loss rate temperature |
| MON | motor octane number |
| PF | wall-flow particulate filter |
| PFI | port fuel injection |
| $R^2$ | coefficient of determination |
| RON | research octane number |
| SOT | starting oxidation temperature |
| TG | thermogravimetric |
| TGA | thermogravimetric analysis |
| VOC | volatile organic compound |

Subscripts

| | |
|---|---|
| $ads$ | adsorption |
| $des$ | desorption |
| $e$ | external |
| $l$ | interparticle |

$ox$ oxidation

$p$ intraparticle

$S$ sorption